Surface modification of titanium substrate via combining photothermal therapy and quorum-sensing-inhibition strategy for improving osseointegration and treating biofilm-associated bacterial infection

Jingwei Hu [a,1], Yao Ding [a,1], Bailong Tao [b], Zhang Yuan [c], Yulu Yang [a], Kun Xu [a], Xuan Li [a], Peng liu [a,*], Kaiyong Cai [a,**]

[a] Key Laboratory of Biorheological Science and Technology, Ministry of Education, College of Bioengineering, Chongqing University, Chongqing, 400044, China
[b] Laboratory Research Center, The First Affiliated Hospital of Chongqing Medical University, Chongqing, 400016, China
[c] Institute of Medical Research, Northwestern Polytechnical University, Xi'an, 710072, China

ARTICLE INFO

ABSTRACT

Insufficient osseointegration and biofilm-associated bacterial infection are important challenges for clinical application of titanium (Ti)-based implants. Here, we constructed mesoporous polydopamine (MPDA) nanoparticles (NPs) loaded with luteolin (LUT, a quorum sensing inhibitor), which were further coated with the shell of calcium phosphate (CaP) to construct MPDA-LUT@CaP nanosystem. Then, MPDA-LUT@CaP NPs were immobilized on the surface of Ti implants. Under acidic environment of bacterial biofilm-infection, the CaP shell of MPDA-LUT@CaP NPs was rapidly degraded and released LUT, Ca^{2+} and PO_4^{3-} from the surface of Ti implant. LUT could effectively inhibit and disperse biofilm. Furthermore, under near-infrared irradiation (NIR), the thermotherapy induced by the photothermal conversion effect of MPDA destroyed the integrity of the bacterial membrane, and synergistically led to protein leakage and a decrease in ATP levels. Combined with photothermal therapy (PTT) and quorum-sensing-inhibition strategy, the surface-functionalized Ti substrate had an antibacterial rate of over 95.59% against *Staphylococcus aureus* and the elimination rate of the formed biofilm was as high as 90.3%, so as to achieve low temperature and efficient treatment of bacterial biofilm infection. More importantly, the modified Ti implant accelerated the growth of cell and the healing process of bone tissue due to the released Ca^{2+} and PO_4^{3-}. In summary, this work combined PTT with quorum-sensing-inhibition strategy provides a new idea for surface functionalization of implant for achieving effective antibacterial and osseointegration capabilities.

1. Introduction

Due to the factors of bone trauma, bone tumor and aging, a large number of orthopedic implant materials are needed in clinic. Orthopedic medical devices have become one of the most important categories in the medical device industry. Titanium (Ti) and titanium alloys have been widely used for biomedical materials in the clinical treatment of human hard tissues such as dentistry and orthopedics, due to their excellent processability, corrosion resistance, low elastic modulus and good biocompatibility [1–3]. However, due to the damage of host immune response caused by surgery, Ti-based implants used for bone tissue repair and replacement are easy to cause bacterial adhesion and then lead to the occurrence of postoperative implant infection, whether long-term use or short-term indwelling in the human body [4–6]. Clinically, orthopedic implant related infections are mainly caused by bacteria in the biofilms. Mature bacterial biofilm can not only adhere to the implant surface, but also penetrate the surrounding tissue and joint cavity [7]. Bacteria in biofilms show high tolerance to host immune system and antibiotic therapy [8]. Once bacterial biofilm is formed, repeated implant replacement surgery and expensive treatment are

---

inevitable, which will bring heavy economic burden to patients. In addition, Ti and its alloys, as bioinert materials, lack the function of "active repair". When Ti-based materials are used for bone tissue repair and replacement, they can't form a firm and long-term bond with the surrounding tissues after implantation. It will eventually lead to implant loosening, which is also an important challenge for their clinical application [9,10]. Therefore, how to endow Ti-based materials with good osseointegration and excellent anti-biofilm infection ability through material design directly determines the success or failure of the operation and long-term service life of the implant.

As the most common and complex complication of orthopedic surgery, implant related biofilm infection has become one of the most challenging problems faced by orthopedic doctors. Biofilm infection first occurs on the surface of implants, which greatly affects the effectiveness, safety and service life of implants in clinical application. In depth understanding of the surface/interface of implants for anti-biofilm design have become the frontier and hot spot in the field of biomedical materials. So far, researchers at home and abroad have successfully developed a variety of methods to inhibit/remove the biofilm on the implant surface [11–15]. Among them, photothermal therapy (PTT) based on near-infrared radiation (NIR) has been paid more and more attention in antibacterial design and eradication of biofilm, due to its advantages of remote, minimally invasive, non-surgical, deep tissue penetration and avoiding the generation of drug-resistant bacteria [16–18]. However, treatment or removal of biofilm infection via PTT usually requires high laser power and local high temperature. High PTT temperature can cause damage to the surrounding normal cells/tissues [19]. In addition, the mature biofilms formed on the surface of implant often have strong resistance and uneven heat distribution inside the membrane, so it is impossible to completely eliminate bacterial biofilm infection by using PTT technology alone [20,21]. Therefore, how to reduce the damage of PTT process to the healthy host cells and tissues around the implant and effectively kill bacteria/eradicate biofilm, is still an urgent problem.

Relevant studies have found that bacterial biofilm resistance to external factors is regulated by its quorum sensing (QS) [22]. QS can affect the communication between bacteria, thus forming biofilm and enhancing its resistance to external conditions. Recent studies have shown that QS system can not only cause the formation of biofilm, but also activate the virulence pathway of bacteria [23]. Therefore, the inhibition of bacterial QS system is a very potential method in the prevention or treatment of bacterial biofilm infection of implants [24]. It has been confirmed that QS inhibitors can effectively reduce the growth of planktonic bacteria and effectively inhibit/disintegrate bacterial biofilms, so as to achieve the effect of treating bacterial infections [25–27]. So, the combination of PTT and the use of QS inhibitor may provide a new idea for eliminating biofilm infection via achieving low-temperature PTT. However, in the case of only residual necrosis or no vascular tissue after implantation, it is difficult for QS inhibitors to reach the interface between implant and bone tissue after systemic metabolism and blood circulation. What's more, QS inhibitors also have certain cytotoxicity. High dose of QS inhibitors will cause serious damage to surrounding cells and cause unnecessary negative effects. Therefore, QS inhibitors should be efficiently and safely delivered to the implant when bacterial biofilm infection occurs, and at the same time selectively act on pathogenic bacteria, which were important for the combined strategy of PTT and QS inhibitors.

Based on the above mentioned, we attempted to construct a nano-delivery system combined PTT with controlled release of QS inhibitor on the surface of Ti implant (Scheme 1). Firstly, mesoporous polydopamine (MPDA) nanoparticles (NPs) were synthesized, which had excellent NIR photothermal properties [28,29]. Secondly, luteolin (LUT) as QS inhibitor was loaded in MPDA NPs to form MPDA-LUT nanosystem. Thirdly, calcium phosphate coating was constructed on the surface of MPDA-LUT NPs by biomimetic mineralization to form MPDA-LUT@CaP NPs. Finally, MPDA-LUT@CaP NPs were anchored on the surface of Ti substrate through the intermediate polydopamine coating.

Furthermore, the modified Ti substrates were hoped to enhance osseointegration and treat biofilm infection (Scheme 2). Under the weak acid environment of biofilm infection, the calcium phosphate shell of MPDA-LUT@CaP NPs immobilized on the Ti substrate was quickly degraded, which could realize the controlled release of LUT and selectively act on bacterial biofilm/pathogenic bacteria. LUT as a natural polyphenol flavonoids is a good natural drug to inhibit the colony effect of bacterial biofilm and has excellent function of inhibiting/dispersing biofilm [30]. Moreover, recent studies indicated that LUT could effectively inhibit the ATPase activity and the expression of alpha toxin of *Staphylococcus aureus* (*S. aureus*) [31], interfere with the synthesis of bacterial cell walls and improve the permeability of bacterial cell membranes in biofilms [32]. Meanwhile, the Ti impants modified with MPDA-LUT@CaP NPs were irradiated with NIR, which also could eliminate biofilm and kill bacteria. Thus, bacterial biofilm could be removed under the combined action of QS inhibitor and PTT stimulation to achieve low-temperature PTT. In addition, Ca^{2+} and PO_4^{3-} were released from the rapid degradation of calcium phosphate coating of MPDA-LUT@CaP NPs triggered by acid condition of biofilm infection, which could promote the growth of bone-related cell and the healing process of bone tissue [33–37]. All in all, a pH and NIR dual-responsive nanosystem combining PTT and controlled release of QS inhibitor was constructed on the surface of Ti implant for improving osseointegration and treating biofilm-associated infection. The present research provides a new strategy for developing new orthopedic implants with antibacterial and osteogenic functions.
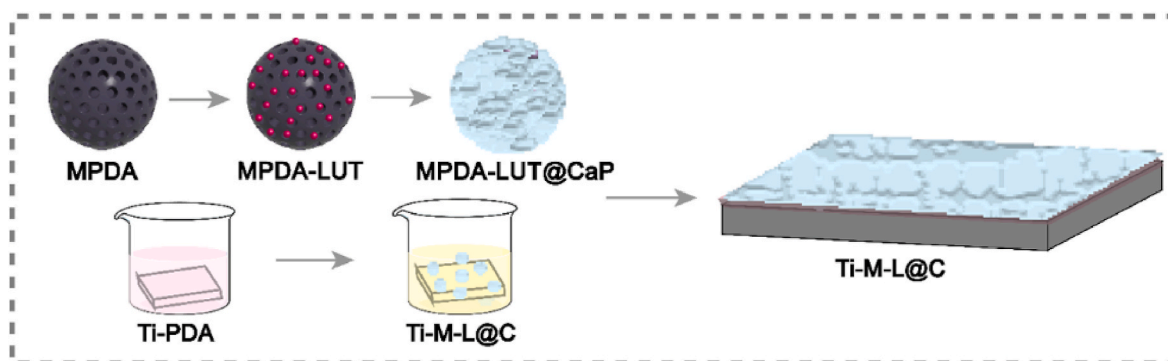
Scheme 1. Schematic diagram the preparation process of Ti-M-L@C substrate.
MPDA: mesoporous polydopamine nanoparticles; LUT: Luteolin; MPDA-LUT: MPDA nanoparticles loaded with LUT; MPDA-LUT@CaP: MPDA-LUT nanoparticles coated with calcium phosphate shell; Ti-PDA: Ti substrate modified with polydopamine; Ti-M
-L@C: Ti substrate modified with MPDA-LUT@CaP nanoparticles.
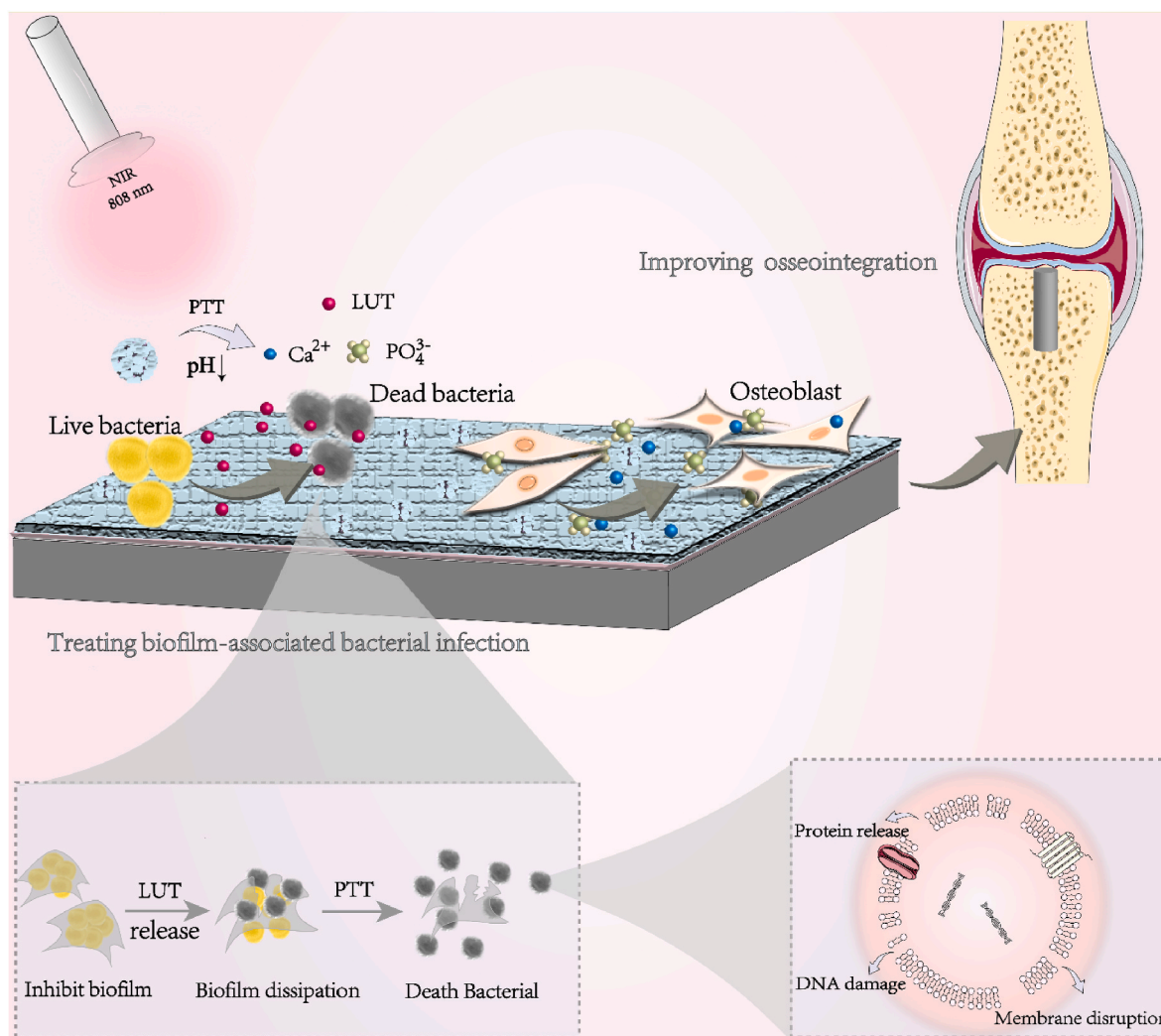
Scheme 2. Schematic diagram of combining PTT and quorum-sensing-inhibition strategy for improving osseointegration and treating biofilm-associated bacterial infection of Ti-based implant.

2. Materials and methods

2.1. Materials

Commercial Ti foils (0.25 mm thick, 99.5% purity) and Ti rods (1.2 mm of diameter, 10 mm of length) were purchased from Alfa Awsar Co. (Tianjin, China) and Northwest Institute for Non-ferrous Metal Research (Shanxi, China), respectively. Medical Ti bone nails (Ti6Al4V, 1.5 mm of diameter, 7 mm of length) was purchased from Yunaosi Co. (Suzhou China). Luteolin with a purity was purchased from Macklin Biochemical Co. Ltd. (Shanghai, China). Dopamine hydrochloride, 1,3,5-trimethyl-benzen (TMB), Tris(hydroxymethyl) aminomethane hydrochloride (Tris-HCl), and Triton X-100 were purchased from Aladdin Industrial Co. (Shanghai, China). Pluronic® F127 was purchased from Sigma-Aldrich Co. (St. Louis, MO, USA). Cell counting kit-8 (CCK-8), alkaline phosphatase (ALP) kit, bicinchoninic acid (BCA) assay kit, and Live & Dead bacterial staining kit were obtained from Beyotime Biotechnology Co. (Jiangsu, China). Other reagents were purchased from Oriental Chemical Co. (Chongqing, China).

2.2. Synthesis of MPDA NPs

According to previous reports of our research group, MPDA NPs were synthesized by one-pot method [11,16,28,29]. A mixture of 65 mL H_2O and 60 mL ethanol was prepared and 0.36 g F127 and 0.36 g TMB were dissolved in the above solution. After stirring and dissolving, 90 mg TRIS solution (10 mL H_2O) was firstly added to the mixture, followed by 60 mg dopamine hydrochloride. The mixture was reacted at room temperature for 24 h, and the product was initially collected. The template was removed by extraction and the synthesized MPDA was collected by high-speed centrifugation. The prepared MPDA NPs were then characterized by transmission electron microscope (TEM).

2.3. Preparation of MPDA-LUT@CaP NPs

The MPDA and LUT were dispersed in a methanol solution at a mass ratio of 1:1.4, and stirred for 24 h for drug loading. LUT is gradually enriched in the mesoporous MPDA by π-π accumulation and hydrophilic/hydrophobic action. The drug-loaded nanoparticles (MPDA-LUT) were collected by centrifugation, and the drug loading was detected by UV–Vis Spectroscopy. MPDA-LUT nanoparticles were dispersed in SBF at a concentration of 0.5 mg/mL. The reaction was stirred at 37 °C for 48 h to induce a CaP coating on the surface of MPDA particles (MPDA-LUT@CaP). Energy dispersive X-ray spectroscopy (EDX), X-ray diffraction (XRD), dynamic light scattering (DLS) and zeta potential detection were employed to confirm the success construction of CaP coating.

2.4. Immobilization of MPDA-LUT@CaP NPs on the surfaces of Ti substrates

The Ti foils (1 cm × 1 cm) were soaked in Tris buffer-HCl solution (pH 8.5, 10 mM) solution containing of dopamine hydrochloride (2 mg/mL) overnight at room temperature to form polydopamine coating. After that, the modified Ti substrates were taken out, washed with three distilled water, and dried. MPDA-LUT@CaP nanoparticles were dispersed in PBS, pH 7.4 at a concentration of 200 μg/mL. The polydopamine-coated Ti substrate was put into the MPDA-LUT@CaP nanoparticles solution and reacted for 24 h. Then, the prepared sample was named as Ti-M-L@C. In addition, MPDA and MPDA-LUT NPs were immobilized on the polydopamine-coated Ti substrate, namely as Ti-M and Ti-M-L. The surface morphologies of different samples were characterized by field emission scanning electron microscope (FE-SEM). X-ray photoelectron spectrometer (XPS) was used to characterize the element composition and crystal of various Ti substrates. The wearness resistance of Ti-M-L@C sample was tested with a friction and wear testing machine (WAZAU TRM 1000, Germany). The bonding strength and modulus of the coating on the Ti substrate were tested by the NanoIndenter XP system (Hysitron TI950, USA) and the nanoscratch option with a mode of controlled indentation depth.

2.5. The release behavior of LUT

Firstly, the cumulative release of LUT of the prepared various samples was studied. The prepared Ti-M-L and Ti-M-L@C samples were incubated at 37 °C in 1 mL PBS solution with pH 7.4 and pH 5.5 respectively. Then the PBS were collected at different time intervals (0, 0.5, 1, 2, 4, 8, 16, 24, 36, and 48 h). Next, the absorbance of LUT of all groups were measured with UV–vis spectroscopy (PECORD®210 PLUS, Analytikjena, German) at the wavelength of 350 nm [30]. Each set was repeated three times, and the release of LUT in different groups was calculated according to the standard curve.

In addition, the structure and activity of LUT under NIR photo-thermal radiation were tested. The Ti-M-L@C samples were placed in 1 mL PBS, and then irradiated with 808 nm laser (1 W/cm^2) for 10 min. LUT released by materials in solution was collected and detacted by UV–vis and Infrared spectrophotometers (Model 6300, Bio-Rad, USA).

2.6. The release behavior of Ca^{2+}

The prepared Ti-M-L@C samples were incubated at 37 °C in 1 mL PBS solution under different pH (pH = 7.4 or 5.5) and with or without NIR irradiation. Then, the PBS were collected at different time intervals (0.5, 1, 2, 4, 8, 12, 24, 72 and 168 h). Next, the cumulative release of Ca^{2+} was detected by an inductive coupled plasma-atomic emission spectroscopy (ICP-AES, Vista AX, Varian, USA). Each set was repeated three times.

2.7. Photothermal property of different Ti substrates

The 808 nm laser (1 W/cm^2) was used to irradiate 1 mL PBS solution with different samples (Ti and Ti-M-L@C) in a 24-well culture plate, and recorded temperature with a thermocouple probe (HH806AU, OMEGA, USA).

2.8. Antibacterial and anti-biofilm activity in vitro

2.8.1. Antibacterial property evaluation in vitro

The gram-positive bacteria S. aureus (ATCC29213) were used to study antibacterial activity of all the samples in vitro. S. aureus was cultured in Luria-Bertani (LB) medium, and the cell concentration was measured by an UV–vis spectroscopy to prepare a bacterial suspension sample with OD$_{600}$=1.0 (10^9 CFU/mL). The in vitro antibacterial effect of native Ti, Ti-M, Ti-M-L and Ti-M-L@C samples against S. aureus was measured with or without 808 nm near-infrared radiation by plate counting method. In a 24-well plate, 1 mL of 1×10^6 CFU/mL bacterial suspension was co-cultured with various samples for 24 h, and then irradiated with 808 nm near-infrared laser (1 W/cm^2, 10 min), respectively. After that, the samples were taken out and put them into sterile PBS solution (1 mL). After sonicating them for 1 min and the bacterial suspension were collected. Afterward, the obtained suspension was diluted for 10,000 times, and 100 μL of above mixture was added to the plate and incubated overnight at 37 °C. A digital camera was used to take images of formative colony forming units (CFU) and the number were counted to assess the antibacterial effect. Antibacterial rate calculation formula: A = (B–C)/B × 100%. A is the antibacterial rate; B is the average CFUs value of the control group (Ti without NIR); C is the average CFUs value of the experimental groups.

2.8.2. Antibiofilm property measurement in vitro

Set up 8 experimental groups to evaluate the anti-biofilm performance of materials: Ti, Ti-M, Ti-M-L, Ti-M-L@C without or with NIR. Place the materials (Ti, Ti-M, Ti-M-L, Ti-M-L@C) in a 24-well plate and add 1 mL of S. aureus bacterial suspension (1×10^8 CFU/mL). The medium was changed every 24 h, and the biofilm was constructed by incubating them at 37 °C for 48 h. 4 groups of NIR + materials were irradiated with 808 nm laser (1 W/cm, 10 min). Remove the upper layer of medium, gently wash away non-adherent bacteria with PBS, and harvest the biofilm co-incubation material.

The crystal violet staining method was used to evaluate the anti-biofilm performance. After various treatment, the formed biofilm were stained with 0.1% crystal violet solution for 10 min. After washing with PBS, 500 μL of ethanol was added into each well to dissolve the stained samples. Lastly, the OD value of biofilm biomass was measured with the spectrophotometric microplate reader (Bio-Rad 680, USA) at 595 nm.

The morphologies of obtained biofilms on all groups were characterized by scanning electron microscopy (SEM). The biofilm were fixed in paraformaldehyde (4 wt %) at 4 °C for 4 h. After that, the samples were dehydrated with ethanol (20, 40, 60, 80, and 100%) continuously for 10 min each time. Lastly, the samples were dried and sprayed with gold, and the bacterial morphologies of the biofilms were observed with SEM.

Live/dead staining was used to observe the formed biofilm 3D laser scanning confocal microscopy (CLSM). The biofilm samples were treated with SYTO9 and PI mixed dyes for 20 min. Bacteria with intact cell membranes show green fluorescence, while damaged bacteria mainly show red fluorescence. Image processing and 3D images compilation were performed under a confocal laser scanning microscope (Leica Microsystems, Germany).

2.8.3. Antibacterial and anti-biofilm activity after storage in vitro

The samples were stored in air, PBS and LB medium for one month to evaluate their antibacterial ability and biofilm elimination ability. In short, we put the samples in a 24-well plate and store them in the air for long-term storage or add 1 mL PBS or LB medium to each sample well for PBS or medium storage. One month later, to evaluate the antibacterial and anti-biofilm efficiency of the samples. The method was the same as the one mentioned above.

2.9. Evaluation of bacteria membrane permeability

The o-nitrophenol-β-D-galactosidase (ONPG) hydrolysis method was used to determine the release activity of β-galactosidase in the bacterial cytoplasm to determine the membrane permeability. ONPG can quickly enter bacterial cells and hydrolyze by intracellular β-galactosidase, releasing of yellow o-nitrophenol (ONP), which has a characteristic absorption peak at 420 nm [11,28,29]. The biofilms were collected from different groups by ultrasound to prepare suspensions of bacterial, and ONPG detection solution (β-galactosidase Assay Kit, Solarbio) as added to each sample. The absorbance of all groups was measured with a

spectrophotometric microplate reader (Bio-Rad 680, USA) at 420 nm.

The integrity of the bacterial cell membrane is evaluated by measuring the OD_{260} value of the supernatant, which reflected the release content of intracellular components. The 1×10^6 CFU/mL bacterial suspension was incubated with various samples for 6 h, and the supernatant was collected after NIR irradiation. After filtering through a 0.22 μm membrane, the absorbance of obtained suspension was measured using UV–Vis spectroscopy at 260 nm.

The changes of ATP concentration of the co-incubated bacteria in each group of materials were assessed to reflect the level of cell metabolism [13]. Typically, the 1×10^6 CFU/mL bacterial suspension was incubated with different substrates for 6 h. After laser radiation, the enhanced ATP detection kit (Beyotime) was used to detect the luminous intensities with Fluorescence spectrophotometer (RF-6000, Daojing, Japan).

2.10. Biocompatibility assessment in vitro

2.10.1. Cytotoxicity and morphological evaluation

The osteoblasts used in the experiment were isolated from the skull of newborn rats, and the third generation osteoblasts were employed in subsequent experiments [16]. The 2×10^4 cells/cm^2 cells were seeded on each group and cultured for 48 h, and then fixed with 4% para-formaldehyde. After permeabilizing with 0.2% TritonX-100, the cellular cytoskeleton was stained with rhodamine-phalloidin overnight, and then the nuclei were stained with Hoechst 33258 for 10 min. Lastly, the cell morphology was observed under a confocal laser scanning microscope (CLSM) (TCS SP5, Leica, Germany).

The CCK-8 method was used to study the cell viability of bare and modified Ti substrates [16]. After putting the samples into 24-well plates, osteoblast suspension (1 mL, 4×10^4 cells/cm^2) were added to each well, and cultured for 1, 4, and 7 days, respectively. When testing, 200 μL of serum-free medium and CCK-8 mixed solution (v/v = 10:1) were added and incubated for 4 h, and then the optical density of each sample at 450 nm were determined with the spectrophotometric microplate reader (Bio-Rad 680, USA).Then, cell viability of different Ti substrates under NIR irradiation (1 W/cm^2, 10 min) for 1, 4, and 7 days were also measured according to the above experimental process. In addition, cell viability analysis for 1, 4 and 7 days cultured on different samples with acidic medium (pH = 5.5) were performed.

2.10.2. Evaluation of alkaline phosphatase (ALP) activity

To detect the ALP activity of all groups, the osteoblasts were inoculated in the same way on different titanium substrates for 4 and 7 days, respectively. Triton X-100 were added to lyse the cells and collected the supernatant. BCA kit and ALP kit were used to determine the total intracellular protein and ALP content in the supernatant, and analyze the ALP activity of various substrates.

2.10.3. Osteogenesis-related gene expression detection

Quantitative real-time PCR (qRT-PCR) was used to analyze the gene expression levels of osteoblasts from the samples. 1 mL of (4×10^4 cells/mL) osteoblasts were incubated with each groupson 24-well plates for 14 days. Then, trizol reagent and RNA extraction kit (Bioteck Co.) were used to extract total RNA on different samples, and then PrimeScriptTM RT kit (Takara Co.) was used for reversing transcription on the Bio-Rad CFX Manager system. The specific primer sequences used in this study were listed in Table S1. Through normalization analysis with the reference β-actin, the expression levels of the osteogenic related genes runt-related transcription factor 2 (Runx2), alkaline phosphatase (ALP), type I collagen (Col I), osteocalcin (OCN), and Osteoprotegerin (OPG) were detected [13,18].

2.11. In vivo study

2.11.1. Implantation surgery

For *in vivo* study, the rat knee joint humeral implant infectious model was established to study the antibacterial effect. All animal experiments and procedures were performed with approval of Animal Ethics Committee of Third Military Medical University. Sprague Dawley (SD) rats (about 250 g) were used and random divided into four groups: Ti NIR-, Ti NIR+, Ti-M-L@C NIR-, Ti-M-L@C NIR+.

Before operation, the rats were anesthetized with 10% chloral hydrate (0.8 mL/100 g) in the abdominal cavity, and the lateral plane of the femur of the left and right legs was exposed. The 1 mm surgical drill was used to create a narrow channel with the diameter of 1.2 mm at the femur. Subsequently, 10 μL of 10^5 CFU/mL *S. aureus* bacterial suspension was injected into the bone injury site. Finally, the bare Ti and modified Ti rods were inserted the implant and the soft tissue and skin were sutured under aseptic conditions. After surgery, 808 nm laser was used to irradiate the femoral implant site for 10 min (d = 1 cm, 1.0 W/cm^2), and the temperature was recorded.

2.11.2. Antibacterial analysis in vivo

After operation for one week, the femurs of the rats were taken out to analyze the infection at the implant site. Firstly, the implant Ti rods were immersed in 5 mL of MHB medium, incubated at 37 °C overnight, and the turbidity was observed. Secondly, the rods were taken out and rolled on the plates directly and incubated overnight, then observed and recorded the growth of bacteria. In addition, the implants were immersed in 1 ml PBS, and then sonicated for 10 min to collect the adhered bacteria of the implants. After the bacterial suspension was diluted for 10 times, the plate coating method was used to determine the number of bacteria on different implants.

2.11.3. Histological analysis

After placing the femurs in the tissue fixative for 72 h, the collected samples were decalcified with ethylenediaminetetraacetic acid (EDTA, 12 wt 9%) solution for 1 month. After that, the implanted Ti rods were taken out, the tissues were gradually dehydrated in ethanol solution, infiltrated with xylene, and embedded in paraffin for sectioning. Then, hematoxylin-eosin (H&E) and Masson staining were performed on these soft tissue sections to assess infection. In addition, to evaluate the applicability of this interface modification method for clinical application of bone nails. We performed the same modification with medical Ti-based bone nails and performed H&E staining to evaluate the new bone in different samples.

In order to further verify the osteogenic ability of the material, after the fixed bone samples were dehydrated by gradient ethanol, transparent, and sealed with 5% BSA at room temperature, the sliced part were prepared and the expressions of OCN and Col I proteins around the new bone were subjected to immunohistochemistry (IHC) staining.

2.11.4. Micro-CT analysis

The micro-CT scanner (SCANCO Medical AG, Viva CT40) was used to evaluate the osseointegration of the tissue around the implant based on the 0.8 mm area around the implant. The humerus tissue was taken out from the body and put into tissue fixative for 48 h. After scanning image reconstruction, quantitative analysis of new bone volume (BV), bone volume/tissue volume (BV/TV), trabecular thickness (Tb.Th), trabecular number (Tb.N), trabecular space (Tb.Sp) and bone density (BMD of BV).

3. Result and discussion

3.1. Synthesis and characterization of different NPs

A one-pot method was used to synthesize MPDA nanoparticles, and the spit hydrochloride monomer was stacked on the interface formed by

Pluronic F127 and 1,3,5-trimethylbenzene (TMB), and finally a hollow mesoporous nanoparticle is formed. Transmission electron microscope imaging (TEM) was used to detect the synthesis of the analyzed particles. TEM shows that the nanoparticles were regular spherical and the surface mesoporous morphology was clear (Fig. S1A). As shown in Fig. S1B, the result of the BET detection data shows that the nitrogen adsorption-desorption curve of particles is an IV-type isotherm according to the IUPAC nomenclature. The specific surface area of MPDA is about 47.8 m^2/g, and the total pore volume is 0.191 cm^3/g. The capillary condensation step with a wider h4 hysteresis loop is observed in the P/P0 range of 0.4–0.8, reflecting that the particles have a wider pore size distribution in the range of 3–30 nm, and the peak pore size is about 3.77 nm (Fig. S1C). Due to the ironically mesoporous structure, there is also a pore size distribution in the range of 5–12 nm. In order to test the photothermal conversion performance of the synthesized MPDA, the temperature change MPDA nanoparticles with different concentrations under 808 nm laser (1 w/cm^2) radiation was measured (Fig. S2A). The results showed that the solution temperature of PBS with a nanoparticle concentration of 100 μg/mL increased by 20.1 °C within 10 min, reaching 48.7 °C. The temperature of the PBS solution with a particle concentration of 200–600 μg/mL can reach 53–60 °C. However, the pure PBS solution only rises by 4.5 °C. According to the MPDA (0.5 mg/mL) photothermal spectra of three near-infrared lasers on/off cycles indicates that the photothermal conversion effect of the particles is stable, and there is no significant deterioration during the repeated cycle (Fig. S2B). According to the recorded heating and cooling curve of MPDA solution, the characteristic thermal time constant and the steady maximum temperature are obtained [11,16], and the photothermal conversion efficiency (η) of MPDA is calculated to be 37%.

After that, the step-by-step drug loading and coating construction and related characterization of NPs were carried out. Luteolin (LUT) has an ultraviolet absorption peak around 350 nm [30,31]. The standard curve of LUT drug concentration measured by ultraviolet spectrophotometry is shown in Fig. S3. After the drug was loaded into MPDA NPs,

the UV absorption value at 350 nm in the remaining solution was measured, and the drug loading rate was calculated to be 71.4%. Subsequently, in order to prevent drug leakage and maintain the ability to respond to bacteria, a pH-responsive calcium phosphate (CaP) coating was used to cover the particle surface. Previous studies have shown that polydopamine, which is rich in catechol groups, has strongly binding property with metal ion of Ca^{2+} in biomineralization [38]. In SBF solution, it can induce the deposition of hydroxyapatite [39]. As shown in Fig. 1A, after modification of CaP layer, TEM image reveals the spherical structure of MPDA-LUT@CaP remains intact and the irregular mesoporous structure of the outer layer is covered. DLS result demonstrates that the particle size of pure MPDA was approximately 250 nm, while the particle size of MPDA-LUT@CaP NPs increased to about 280 nm (Fig. 1B). The zeta potential measurement also observed that MPDA-LUT@CaP carries more negative charges, revealing the construction of the negatively charged CaP coating on the outer layer (Fig. 1C). Wide-angle XRD detection showed that MPDA-LUT@CaP exhibited characteristic peaks consistent with hydroxyapatite (HA) at 211 and 002 (Fig. 1D). The above results demonstrated that MPDA-LUT@CaP NPs were successfully prepare by the formation of surface mineralization.

3.2. Construction and characterization of the modified Ti substrates

A polydopamine coating was formed on the surface of Ti substrate by self-polymerization of dopamine. Then, three kinds of NPs (MPDA, MPDA-LUT, and MPDA-LUT@CaP) were anchored on the surfaces of polydopamine modified Ti substrates respectively to construct Ti-M, Ti-M-L, and Ti-M-L@C sample. The catechol functional group of polydopamine can bind to calcium phosphate and hydroxyapatite. Based on this, polydopamine was used as the intermediate layer for immobilizing MPDA-LUT@CaP NPs on the surface of Ti implant [40–42]. The immobilization of NPs on the surface of Ti material was observed by SEM. As shown Fig. 2A, the particles were evenly distributed on the
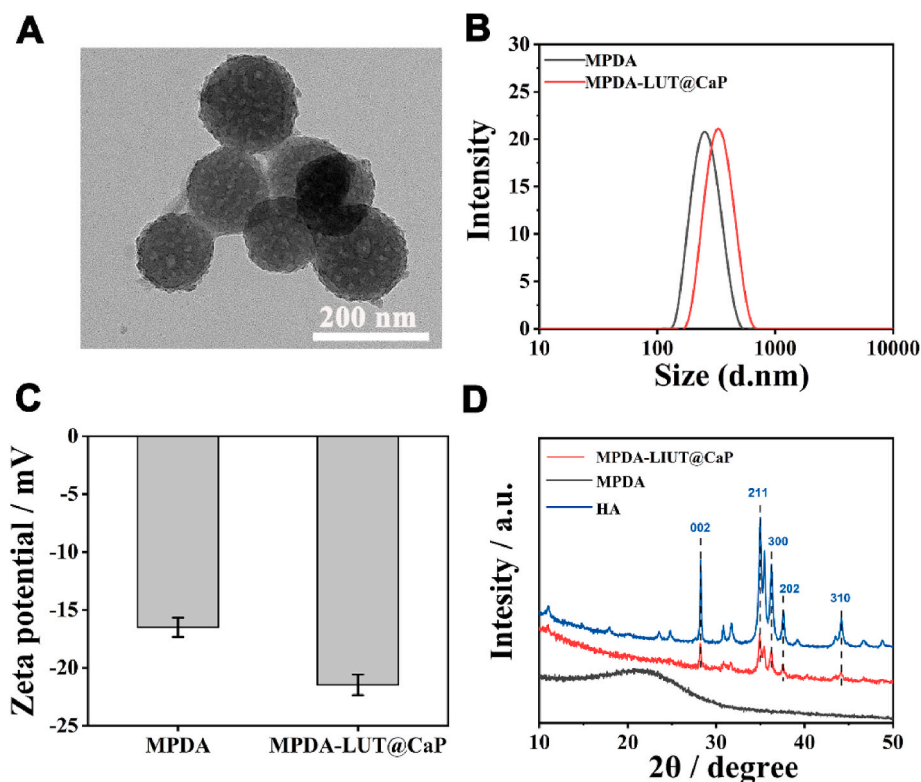
Fig. 1. (A) TEM image of MPDA-LUT@CaP NPs; (B) DLS inspection image of MPDA and MPDA-LUT@CaP NPs; (C) Zeta potentials of MPDA and MPDA-LUT@CaP NPs; (D) Wide-angle XRD patterns of HA, MPDA, and MPDA-LUT@CaP samples.
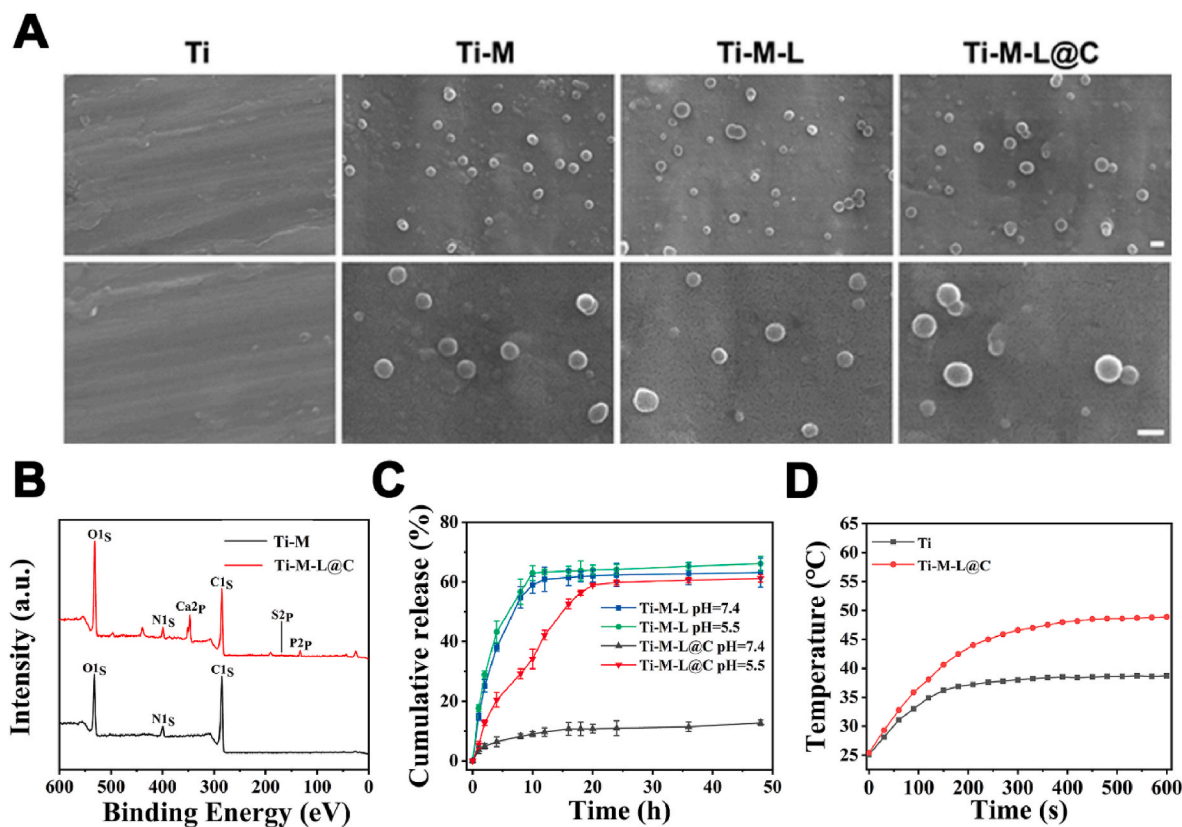
Fig. 2. (A) SEM image of Ti, Ti-M, Ti-M-L and Ti-M-L@C samples, scale bar = 200 nm; (B) XPS survey scan of Ti, Ti-M-L@C samples; (C) Drug responsive release profile of Ti-M-L and Ti-M-L@C samples (n = 3); (D) Thermal curve of Ti and Ti-M-L@C samples.

material surface. The results of XPS analysis of Ti-M-L@C sample revealed that there were features characteristic peaks of Ca2p and P2p (Fig. 2B), indicating successful immobilization of MPDA-LUT@CaP NPs. In addition, the properties of coating of Ti-M-L@C substrate were studied. The friction coefficient of Ti-M-L@C substrate was about 0.6 (Fig. S5). From Fig. S6, the elastic modulus of the coating was about 18.92 GPa and the bond strength was about 32.16 μN determined by the NanoIndenter.

Subsequently, considering that microenvironment of bacterial biofilm infection is weakly acidic, the pH-responsive release of LUT from the modified Ti substrates was tested (Fig. 2C). The result showed that no matter in a solution with a pH of 7.4 or 5.5, the drug released quickly from Ti-M-L samples (MPDA-LUT NPs modified Ti substrates) and the drug release basically reached the peak within 10 h. However, the Ti-M-L@C sample (MPDA-LUT@CaP NPs treated Ti substrates) only released 10.75% with 16 h in PBS with pH 7.4. In the PBS with pH 5.5, due to the degradation of the CaP shell, the LUT achieved the slow release. The release volume was about 34% at 10 h and the release amount reached the maximum releasing volume (58.98%) at 20 h. The results showed that the CaP coating has good drug blocking effect and pH-responsive release function.

Furthermore, the cumulative release of calcium ions from Ti-M-L@C substrate was also investigated. As shown in Fig. S7A, the release amount of Ca^{2+} from Ti-M-L@C substrate under pH = 5.5 was more than that of the ones under the neutral pH environment (pH 7.4). It meant that the dissolution of the CaP coating was accelerated in acid environment. In addition, the release amount of calcium ions was also promoted, when the Ti-M-L@C substrate was exposed to NIR irradiation. However, the effect of NIR irradiation on the release of Ca^{2+} was much lower than that of acidic conditions.

After that, the temperature changes of the Ti substrates treated with NIR were measured (Fig. 2D). It was found that the temperature of the native Ti sample only increased to 35.6 °C with NIR for 10 min. However, the temperature of the Ti-M-L@C sample was about 48.5 °C after irradiated by near-infrared for 7 min. It reveals that Ti-M-L@C sample remained good photothermal conversion and could be employed antibacterial/antibiofilm applications.

3.3. Characterization of antibacterial properties in vitro

3.3.1. Antibacterial performance evaluation of the modified Ti substrates

Based on the above material design and preparation, antibacterial properties of the modified Ti substrates were evaluated *in vitro*. The antibacterial effect of each group with or without NIR was evaluated with the plate coating method [11]. As shown in Fig. 3A and B, in the absence of NIR irradiation, the antibacterial rate of the Ti-M group was only about 40%. With NIR treatment, the antibacterial rate of Ti-M sample was about 66.8%. However, Ti-M-L and Ti-M-L@C without NIR treatment showed high antibacterial activity, 81% and 77% antibacterial rates due to the release of LUT. LUT had an inhibitory effect on the adhesion and growth of bacteria because it affected the exchange of QS signals outside the bacteria, which hinders the self-protection mechanism of bacteria to a certain extent [43–45]. Furthermore, after NIR laser treatment, the antibacterial rates of Ti-M-L and Ti-M-L@C samples could reach 95.99% and 95.59%, respectively. Previous studies indicated that LUT also affected the structure of bacterial membranes and lead to a more sensitive state [30]. Thus combined with PTT under NIR irradiation, Ti-M-L and Ti-M-L@C could achieve an efficient sterilization effect.

To evaluate the long-term storage ability of the material, the samples were stored in air, PBS and LB medium for one month and then evaluated their antibacterial ability (Fig. S8). As shown in Fig. S8 after stored in air, PBS and LB medium for a long time, the stability and the antibacterial effect of the material was almost unaffected.
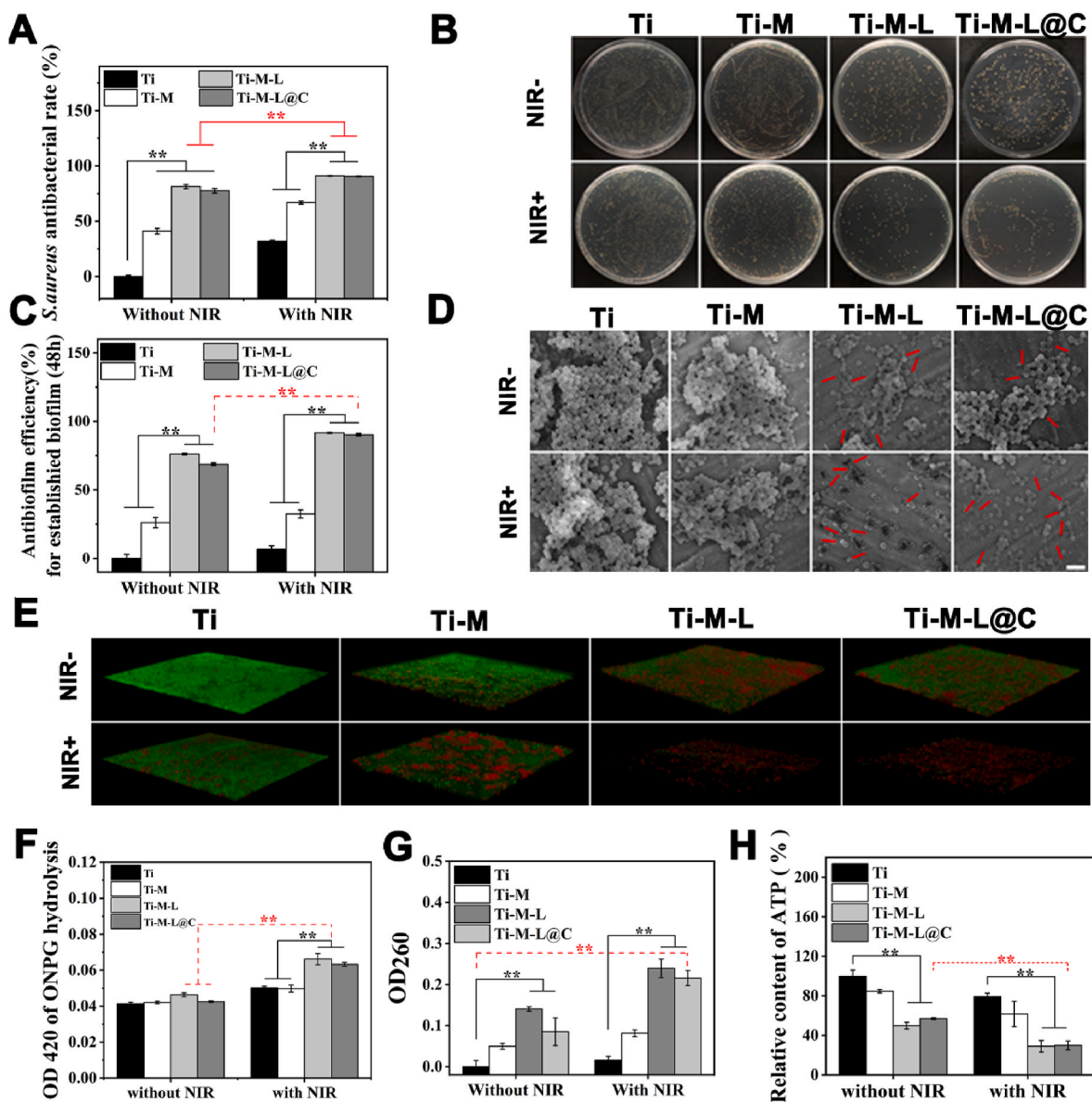
Fig. 3. Antibacterial properties evaluation *in vitro*. (A) Evaluation of antibacterial effect of *S. aureus* on different substrates for 24 h with or without NIR irradiation and (B) representative image of colony activity of *S. aureus* detected by plate smearing method; (C) Normalized analysis of CV stained biofilm; (D) FE-SEM images of biofilms co-incubated on different groups for 48h with or without NIR irradiation, scale bar = 2 μm; (E) 3D confocal laser scanning microscope (CLSM) images of biofilms co-incubated on surfaces of different materials for 48h with or without NIR irradiation. Image sizes: 315.76 μm × 315.76 μm, thickness: 30 μm; (F) The membrane permeability of *S. aureus* was determined by ONPG hydrolysis method; (G) The cytoplasmic content of *S. aureus* released under different treatments; (H) The total ATP level of *S. aureus* adhesion on the surface of various substrates under different treatments. All experiments data comes from 3 independent experiments (n = 3), $*p < 0.05$, $**p < 0.01$.

3.3.2. Assessment of anti-biofilm capacity

Subsequently, Ti, Ti-M, Ti-M-L and Ti-M-L@C samples were cultured with *S. aureus* for 48 h to form biofilm, and the biomass was tested to evaluate the anti-biofilm performance of each sample. According to the crystal violet (CV) staining [11,29], the anti-biofilm efficiency of each group with or without NIR irradiation was evaluated (Fig. 3C). The normalization of staining results showed that the biofilm inhibition efficiency of Ti-M, Ti-M-L, and Ti-M-L@C groups without NIR irradiation reached 26.1%, 76.1%, and 68.7%, respectively. Under NIR treatment, the inhibition efficiency reached 32.4%, 91.6%, and 90.3% respectively. Interestingly, the anti-biofilm effect of Ti-M group did not increase significantly with NIR hyperthermia treatment. However, Ti-M-L and Ti-M-L@C could easily realize the strong inhibition of biofilm without NIR irradiation. This phenomenon further confirmed that LUT, as a natural QS inhibitor, had a high inhibitory effect on the formation of

bacterial biofilms and a negative effect on the status of bacteria. Then, combined with PTT treatment, a better anti-biofilm effect could be achieved.

The long-term biofilm resistance of the samples was also estimated via CV staining method. The results showed that the anti-biofilm efficiency of the samples stored in air and PBS was almost unchanged (Fig. S9).

In addition, FE-SEM was used to observe the adhesion and growth of biofilms on different substrates and the morphology of bacteria (Fig. 3D). It was found that *S. aureus* adhered tightly on the surface of the native Ti substrate and continued to accumulate, thus forming a thicker biofilm. After NIR irradiation, there was almost no negative effect on the morphology of bacteria in the biofilm on Ti sample. However, for the Ti-M with NIR group, the growth and adhesion of bacteria relatively reduced. It could be ascribed to the local high temperature generated by

MPDA NPs during NIR irradiation, which leaded to bacteria death. Although the total volume of the biofilm reduced, the morphology of individual bacteria remains normal, because the bacteria in the biofilm were relatively resistant to external factors. In contrast, for the Ti-M-L and Ti-M-L@C groups, the formation of biofilms were greatly inhibited without NIR treatment and bacterial adhesion significantly reduced. The surface and edge of bacteria presented abnormal morphology and ruptured membrane. After NIR irradiation, the biomass of bacteria greatly decreased and only a small amount of bacteria randomly adhered to the surface. It was found that bacterial morphology presented broken membrane and the contents were leaked. Thus, Ti-M-L and Ti-M-L@C samples with NIR treatment had extremely serious inhibitory and destructive effects on the bacterial biofilms.

In addition, live and dead staining test results also confirmed similar inhibitory effect of biofilm (Fig. 3E). After 3D reconstruction of images, it was found that the biomass on the surfaces of Ti and Ti-M groups were relatively thicker, and there were more living cells. For the Ti-M-L and Ti-M-L@C groups without NIR irradiation, the amount of biofilm was thinner. After NIR irradiation treatment, the adherent cells were significantly reduced and the staining bacteria were almost presented red fluorescence. It was demonstrated that PTT combined with LUT-QS inhibitor could significantly reduce the thickness of the biofilm. Therefore, Ti-M-L@C had a good therapeutic potential in inhibiting and killing biofilms.

3.3.3. Investigation of antibacterial mechanism

Based on the above results, damage verification and antibacterial mechanism on the bacteria incubated with each group were conducted. First, o-nitrobenzene β-D-galactopyranoside (ONPG) hydrolysis method was used to study the permeability of the bacterial membrane. Previous studies have verified that once the bacterial membrane was severely damaged, exogenous ONPG could effectively penetrate into the damaged bacteria and combine with intracellular β-galactosidase to catalyze the production of o-nitrophenol. The o-nitrophenol has a characteristic absorption peak at 420 nm, and the value of its absorption peak could reflect the permeability of the bacterial membrane [11,16]. As shown in Fig. 3F, before NIR irradiation, the degree of hydrolysis of ONPG in each group was similar. For Ti and Ti-M groups with NIR treatment, the hydrolysis level of ONPG slightly increased. However, the hydrolysis level of Ti-M-L and Ti-M-L@C samples significantly increased, which indicated that the cell membrane was more vulnerable to PTT treatment due to the effect of released LUT. LUT inhibited bacterial QS and had a synergistic effect with PTT treatment.

Subsequently, we detected the cytoplasmic leakage of the co-incubated bacteria, with OD_{260nm} measurement as a quantitative indicator [11,16,46]. Once the bacterial membrane was damaged, the intracellular contents including DNA and RNA were released uncontrollably, which could affect the normal physiological activities of bacteria. In the absence of NIR irradiation, the bacterial cytoplasm leaked significantly in the Ti-M-L group (Fig. 3G), which could be due to the release of the LUT, damaging the bacterial membrane and leading to fracture of cell membrane. The relatively low concentration of OD_{260nm} in Ti-M-L@C group might be due to the blocking effect of the outer CaP shell. Moreover, the effect of LUT on cell membrane is a long-term physiological process. The LUT released from Ti-M-L@C sample was pH-reponsvie and the action time was shorter than that of Ti-M-L group. However, in the presence of NIR irradiation, it was found that the level of bacterial content leakage of the Ti-M-L@C group significantly increased, suggesting that the synergistic effect of PTT could cause instantaneous destructive damage to the bacteria.

Adenosine triphosphate (ATP) also is one kind of the leakage of bacterial contents [47,48]. Therefore, after different treatment conditions, the total ATP content of bacteria on different Ti substrates was shown in Fig. 3H. It was worth noting that after NIR irradiation, the total amount of bacterial ATP in the Ti-M-L and Ti-M-L@C groups significantly decreased, which proved that the cell membrane was obviously

damaged and the physiological metabolism of the bacteria was also affected.

3.4. Biocompatibility characterization in vitro

The cytocompatibility of each sample was studied to verify the application prospects in surgical implantation of bone injuries. Osteoblasts were cultured on Ti, Ti-M, Ti-M-L, Ti-M-L@C for 1, 4, and 7 days. Then, CCK-8 assay and fluorescent staining were performed to evaluate the cytocompatibility of different Ti substrates [11,16]. As shown in Fig. 4A. Obviously, after one day of culture, the cell viability of Ti-M, Ti-M-L and Ti-M-L@C was lower than that of Ti group. With the extension of the culture time, by 7 days, the cell activity of Ti-M and Ti-M-L@C groups increased significantly and remained consistent with Ti sample. However, the Ti-M-L group was always lower than the other three groups. After 1 day culture, the lower cell activity of Ti-M, Ti-M-L and Ti-M-L@C may be due to the immobilization of NPs that changed the topography of the Ti surface, which affected the early cell adhesion. In contrast, the cell activity of the Ti-M-L group was consistently lower than others, mainly because the rapid release of high-concentration LUT had certain cytotoxicity and a negative impact on the normal physiological activities of the cells. To a certain extent, the shell of the CaP coating effectively controlled the burst release LUT, which reduced the toxicity of the Ti-M-L@C group to osteoblasts.

Under NIR irradiation, the viability of cell grown on Ti, Ti-M, Ti-M-L and Ti-M-L@C substrates was detected after culture for 1 and 4 days (Fig. S10). The results showed that the cell viability of Ti-M-L@C samples was improved compared with those of Ti, Ti-M, Ti-M-L substrates. Furthermore, the activity of cells in a bacterial infection environment was evaluated, we use acidic medium (pH 5.5) to simulate the infection microenvironment. As shown in Fig. S11, the fabricated Ti-M-L@C substrate presented good cytocompatibility. In our opinion, the cell activity of Ti-M-L@C substrates was higher that of other groups, which was attributed to the release of Ca^{2+} and PO_4^{3-} under acidic conditions and NIR irradiation.

Subsequently, CLSM was used to observe the adhesion of cells incubated for 1 day on different Ti substrates. After staining with rhodamine-phalloidin and H33258, the cell skeleton and nucleus showed red and blue fluorescence, respectively. Without NIR irradiation, the status of cell adhesion was consistent with the cell viability test results. The Ti-M-L group had obvious shrinkage, while the Ti-M-L@C group had more pseudopodia extension (Fig. 4B). After NIR irradiation, there was no obvious difference in cells adhered on Ti, Ti-M and Ti-M-L@C groups. However, the number of cell adhesion in the Ti-M-L group decreased and the shrinkage became more serious with abnormal morphological change at the edge of the cells. This results demonstrated that the existence of the hydroxyapatite-like properties of CaP coating provided the blocking effect of LUT and reduced it's negative impact on osteoblasts. Previous studies have shown that HA has a chemical composition and structure similar to bone tissue, and has good biological activity and compatibility, which could benefit for early osseointegration [49,50]. Osteoblasts in Ti-M-L@C group presented the smooth spreading may be due to bioactivity of CaP. The spreading of cells and the extension of pseudopodia were conducive to the transmission of information between cells, which had advantages in early osseointegration.

Furthermore, ALP activity was used as an indicator to evaluate the early differentiation of osteoblasts of each samples [51,52]. After culture for 4 and 7 days, the ALP activity of the Ti-M-L@C was higher than that of Ti and Ti-M-L ($p < 0.05$ or $p < 0.01$) (Fig. 4C). So, the shell of the CaP coating overcame the negative effects of LUT on cells and further promoted the early differentiation of osteoblasts. In addition, there were no significant difference between Ti-M-L@C and Ti-M samples. It was demonstrated that the components of MPDA could benefit for osteogenic differentiation according to the previous study [53].

RT-qPCR was used to analyze the expression level of osteogenic
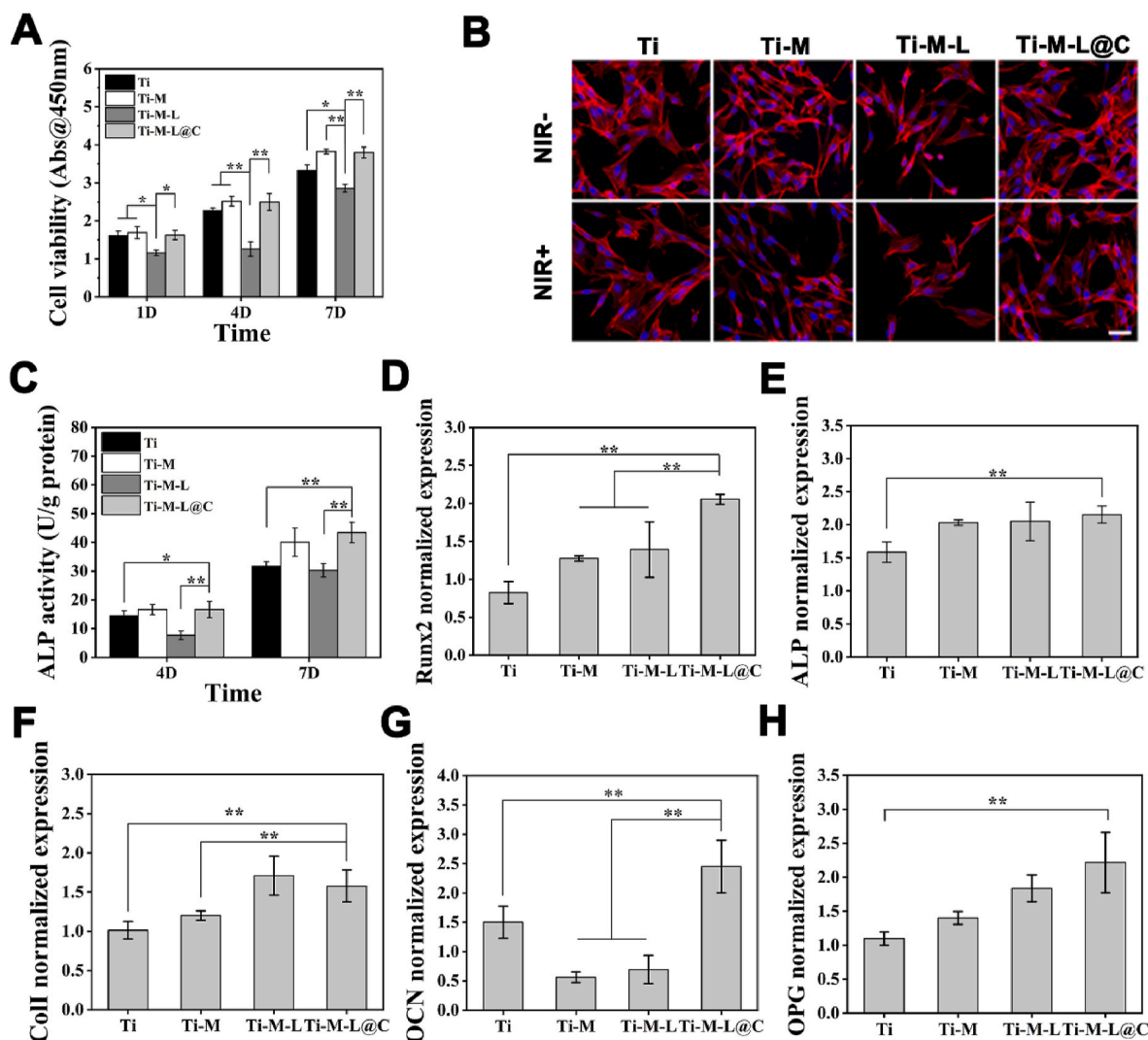
Fig. 4. Cytocompatibility characterization *in vitro*. (A) Cell viability analysis for 1, 4 and 7 days cultured on each group; (B) CLSM imaging for analysis of early osteoblast adhesion in different treatments, scale bar = 50 μm; (C) Alkaline phosphatase activity analysis for 4 and 7 days; Osteogenesis-related specific gene expression level analysis of osteoblasts cultured on different groups: (D) Runx2, (E) ALP, (F) Col I, (G) OCN, and (H) OPG. All experiments data comes from 3 independent experiments (n = 3), *$p < 0.05$, **$p < 0.01$.

marker genes [11,51,52]. The expression levels of Runx2, ALP, Col I, OCN, and OPG were evaluated after incubation for 14 days (Fig. 4D–H). The results showed that Runx2 was actively expressed in the Ti-M-L@C group, which was significantly higher ($p < 0.01$) than that of other groups. Importantly, it was confirmed that Runx2 as the central regulatory gene has a positive effect on the expression of downstream regulatory genes (ALP, Col I, and OCN) and controls bone formation. The expressions of ALP, Col I, and OCN in Ti-M-L@C group were also remarkably higher ($p < 0.01$) than those in Ti group. In addition, OPG, as an osteoclast inhibitor, was actively expressed in the Ti-M-L@C group. The above results confirmed that Ti-M-L@C promoted the early osteogenic differentiation of osteoblast.

3.5. Assessment in vivo

3.5.1. Antibacterial test and characterization in vivo

Based on the excellent antibacterial properties and the advantages of promoting osteogenic differentiation of Ti-M-L@C sample *in vitro* experiments, it's implantation potential *in vivo* was further evaluated. Firstly, the Ti (as control) and Ti-M-L@C rods were implanted into the infection models, 808 nm laser was used to irradiate the implantation sites in the rat. Meanwhile, the real-time photothermal temperature

change was recorded with the thermal imaging device (Fig. 5A). After NIR irradiation for 10 min, it was observed that the temperatures of Ti and Ti-M-L@C groups reached 38.9 °C and 52.9 °C, respectively, indicating that the Ti-M-L@C group with excellent photothermal effect.

One week after the operation, the humerus of the experimental rats was taken out to evaluate the antibacterial effect. Firstly, the results of the MHB liquid co-cultivation test with each group of implants are shown in Fig. 5B. Obviously, the co-cultured bacterial suspension of the Ti-M-L@C with NIR group was clear, while the Ti group was turbid. It was preliminarily judged that the bacterial growth in the infected part of the Ti-M-L@C with NIR group was significantly inhibited. Subsequently, a rolling test of the implants on the plate found that the number of bacteria attached to the Ti-M-L@C with NIR group was significantly less than that of Ti without NIR group (Fig. 5C). Then, the bacteria on the implants of each group were collected, diluted and quantified by the plate infiltration method (Fig. 5D and E). Compared with Ti without NIR group, the antibacterial efficiency of Ti-M-L@C without NIR group reached 59.9%. While the antibacterial efficiency of Ti-M-L@C with NIR group was as high as 96.1%. In summary, the functionalized structure on the surface of Ti-M-L@C implant has a significant therapeutic effect on the infected site. Combined with NIR irradiation, it can effectively kill the *S. aureus* and realize the excellent antibacterial efficiency.
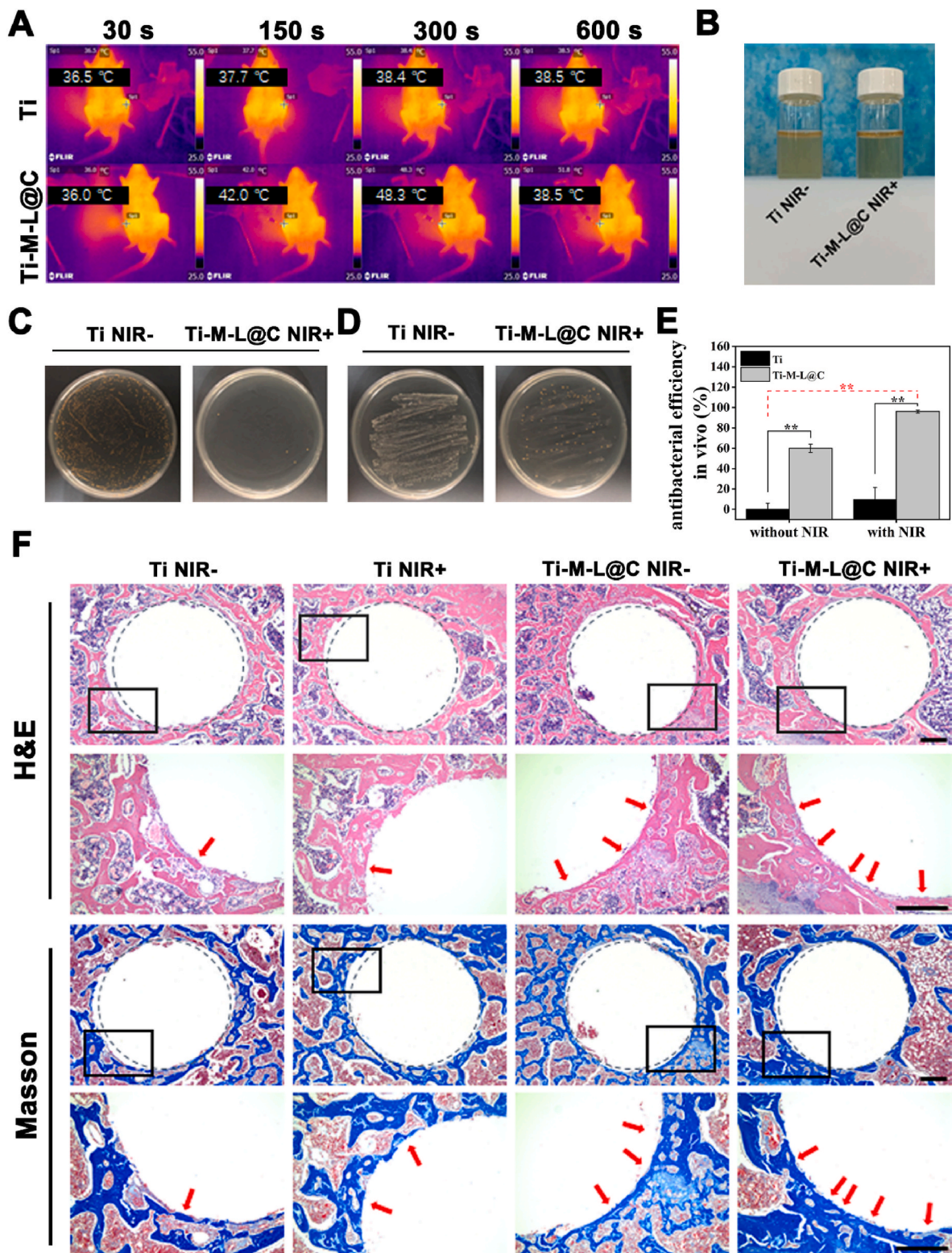
Fig. 5. (A) Thermal images of the real-time temperature of Ti and Ti-M-L@C implants in the humerus after 30, 150, 300 and 600 s of laser irradiation: Ti 36.5 °C, 37.7 °C, 38.4 °C, 38.5 °C and Ti-M-L@C 36 °C, 42 °C, 48.3 °C, 51.8 °C, respectively. (B) Intuitive enrichment culture experiment of *S. aureus* on implants in Ti without NIR and Ti-M-L@C with NIR groups taken from different rats; (C–D) Representative images of Ti without NIR and Ti-M-L@C with NIR implants from different rats rolling on the plate and quantization by plate penetration method; (E) Evaluation of plate infiltration method to quantify antibacterial performance *in vivo*. (F) Histological evaluation of osseointegration after 4 weeks of implantation *in vivo*. H&E and Masson trichromatic staining images of new bone generated around implants in different groups. Gray dotted circles indicate implant edges and osteogenic locations. Black rectangles represent the enlarged image areas. Red arrows indicate new bone formation around the implants. Scale bar = 300 μm. All experiments data comes from 3 independent experiments (n = 3), *$p < 0.05$, **$p < 0.01$. (For interpretation of the references to color in this figure legend, the reader is referred to the Web version of this article.)

3.5.2. Osseointegration assessment in vivo

After surgical implantation, in order to resist exogenous injury and infection in the affected area, the body will rapidly enrich inflammatory cells to reach the implant site, causing related immune activities in surrounding tissues.

After the operation for 4 weeks, the rat humerus implant was removed, and the surrounding tissues were analyzed by hematoxylin-eosin (H&E) and Masson's tricolor staining to observe and count the level of tissue regeneration (Fig. 5F). According to the results, thicker bone-like tissue could be seen around the implants, and the thickness of the new bone tissue formed could be observed by staining images. In the low-magnification images, we found that the Ti samples with or without NIR (Ti NIR+ and Ti NIR groups) had weaker signs of new bone formation on the implant surface. Moreover, the edges of the bone defect are larger than the edges of the implants, indicating that the host tissue is not tightly connected to the implants. For Ti-M-L@C NIR- and Ti-M-L@C NIR+ groups, there were a large areas of newly generated bone tissue around the implants. The fusion of implants and host improved

obviously and the cavity around implants reduced. The enlarged image showed that the Ti-M-L@C NIR- and Ti-M-L@C NIR+ groups had thicker new bone formation, and the Ti-M-L@C NIR+ group was even better. The analysis results showed that the exogenous infection led to the adhesion and proliferation of the bacteria on the surface of the implants. The Ti groups had no antibacterial ability, which hindered the fusion of the implant and host tissue, thus seriously affecting the later bone defect repair and new bone generation. However, for the Ti-M-L@C NIR+ group, due to the antibacterial properties from the released LUT and NIR irradiation, it effectively fought against the infection and inflammation *in vivo*, which promoted the later tissue repair and new bone formation on the surface of implants.

To further investigate the expression of osteogenesis-related proteins around implants in different groups, immunohistochemical staining was performed. Osteocalcin (OCN) and collagen I (COL I) were selected for this study. As shown in Fig. S12, the brown-yellow regions represent regions that are stained positive for different proteins. It can be clearly found that OCN and COL I have the highest expression levels in the Ti-M-
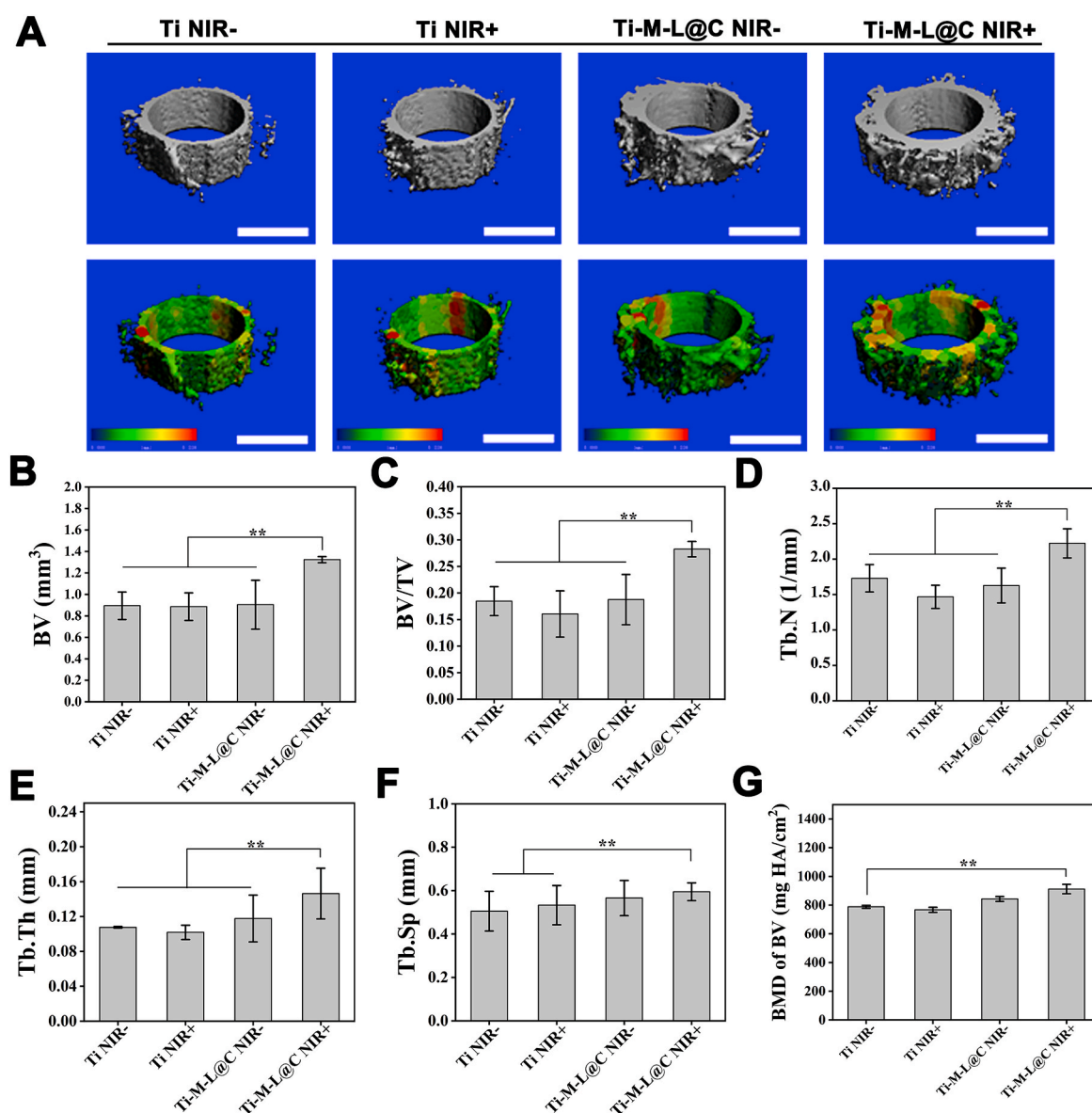
Fig. 6. Evaluation of the effect of bone repair around the different implants. (A) Micro-CT 3D reconstruction images of new bone formation and surrounding trabecular thickness after implantation for 4 weeks (scale bar = 1 mm); Quantitative analysis of (B) new bone volume (BV), (C) bone volume/tissue volume (BV/TV), (D) trabecular number (Tb.N), (E) trabecular bone thickness (Tb.Th), (F) trabecular space (Tb.Sp) and (G) Bone density (BMD of BV) around different implants. All experiments data comes from 3 independent experiments (n = 3), *$p < 0.05$, **$p < 0.01$.

L@C (NIR+) group. The pure titanium group had the lowest expression. However, there was little difference in the expression of these proteins among Ti NIR-, Ti NIR+ and Ti-M-L@C NIR-groups.

After implantation for 4 weeks, the Micro-CT data of the new bone tissue around the implant was shown in Fig. 6. Firstly, the apparent properties of surrounding new bone were analyzed from the 3D reconstructed image (Fig. 6A). It can be clearly found that after NIR treatment, the volume of new bone in the Ti-M-L@C group was significantly larger ($p < 0.01$) than that in the control group. Next, the quantitative analysis of new bone volume (BV), bone volume/tissue volume (BV/TV), trabecular number (Tb.N), trabecular thickness (Tb.Th), trabecular space (Tb.Sp), and bone density (BMD of BV) around the implants were performed. It were found that the amount of BV in the Ti-ML@C with NIR group was significantly greater ($p < 0.01$) than other three groups (Fig. 6B), while the trend of BV/TV, TB.N, Tb.Th (Fig. 6C–E) was consistent with the trend of new bone volume. It was revealed that Ti-M-L@C with NIR group exhibited excellent osseointegration ability. In the analysis of Tb.S and BMD of BV (Fig. 6F and G), it was found that the Ti-M-L@C with NIR group also showed a better trend than other groups. All in all, it can be inferred that the Ti-M-L@C group implants cooperated with PTT treatment, it can fight the inflammation of the infection site and reach the early osseointegration stage due to its excellent antibacterial ability, which led to a more pronounced osteogenesis effect.

To evaluate the applicability of this interface modification method for clinical application bone nails. Clinically used Ti-based bone nail were treated with the same procedure and H&E staining was performed to evaluate the new bone in different samples. As shown in Fig. S13, the black box was the implantation site of bone nail. The new bone formation could be clearly seen in each group along the direction of the screw thread. Meanwhile, Ti-M-L@C NIR+ group showed the most bone formation. And the new bone and native bone in the Ti-M-L@C NIR+ group were more compactly stacked. In a word, all the results showed that the surface-modified implant after NIR irradiation effectively enhanced the formation of new bone.

4. Conclusion

In summary, for the first time, a surface-functionalized Ti-based implant with a nano-delivery system combined PTT with controlled release of QS inhibitor was successfully constructed. Triggered by the weak acid environment of biofilm infection, LUT (a QS inhibitor) was controlled release and selectively act on bacterial biofilm/pathogenic bacteria, which hindered the communication of bacterial QS signals and made them in a sensitive state. Meanwhile, the modified Ti implants were irradiated with NIR, which also could eliminate biofilm and kill bacteria. Thus, bacterial biofilm could be removed under the combined action of QS inhibitor and PTT stimulation. Furthermore, the release of Ca^{2+} and PO_4^{3-} from the surface of implant ensured the biocompatibility in the application of bone implantation and the potential to promote osteogenic differentiation in the later stage. In a word, the combined strategy of QS inhibitor and PTT treatment proposed in this study provides a new idea for fabricate orthopaedic implant with antibacterial and osteogenic function, which will greatly reduce the risk of postoperative infection and secondary surgery.

Declaration of competing interest

Authors have no conflict of interest to declare.

CRediT authorship contribution statement

Jingwei Hu: Conceptualization, Investigation, Data curation, Writing – original draft. **Yao Ding:** Conceptualization, Investigation, Data curation, Writing – original draft. **Bailong Tao:** Investigation. **Zhang Yuan:** Discussion. **Yulu Yang:** Data curation. **Kun Xu:** Investigation, Data curation. **Xuan Li:** Investigation, Discussion. **Peng liu:**

Conceptualization, Revision, Funding acquisition. **Kaiyong Cai:** Conceptualization, Revision, Funding acquisition.

Appendix A. Supplementary data

Supplementary data to this article can be found online at https://doi.org/10.1016/j.bioactmat.2022.03.011.

References

[1] Q.Z. Chen, G.A. Thouas, Metallic implant biomaterials, Mater. Sci. Eng. R Rep. 87 (2015) 1–57.
[2] R. Tejero, E. Anitua, G. Orive, Toward the biomimetic implant surface: biopolymers on titanium-based implants for bone regeneration, Prog. Polym. Sci. 39 (7) (2014) 1406–1447.
[3] C. Hu, D. Ashok, DR. Nisbet, V. Gautam, Bioinspired surface modification of orthopedic implants for bone tissue engineering, Biomaterials 19 (2020) 119366.
[4] Z. Yuan, Y. He, C.C. Lin, P. Liu, K.Y. Cai, Antibacterial surface design of biomedical titanium materials for orthopedic applications, J. Mater. Sci. Technol. 78 (2021) 51–67.
[5] H.C. Flemming, J. Wingender, U. Szewzyk, P. Steinberg, S.A. Rice, K.S. Staffan, Biofilms: an emergent form of bacterial life, Nat. Rev. Microbiol. 14 (2016) 563–575.
[6] H.S. Joo, M. Otto, Molecular basis of in vivo biofilm formation by bacterial pathogens, Chem. Biol. 19 (2019) 1503–1513.
[7] R.M. Pinto, R. Lopes-de-Campos, M.C.L. Martins, P.V. Dijck, C. Nunes, S. Reis, Impact of nanosystems in Staphylococcus aureus biofilms treatment, FEMS (Fed. Eur. Microbiol. Soc.) Microbiol. Rev. 43 (6) (2019) 622–641.
[8] I. Yelin, R. Kishony, Antibiotic resistance, Cell 172 (2018) 1136.
[9] D.D. Bosshardt, V. Chappuis, D. Buser, Osseointegration of titanium, titanium alloy and zirconia dental implants: current knowledge and open questions, Periodontology 73 (1) (2016) 22.
[10] F.A. Shah, P. Thomsen, A. Palmquist, Osseointegration and current interpretations of the bone-implant interface, Acta Biomater. 84 (2019) 1–15.
[11] Z. Yuan, B.L. Tao, Y. He, J. Liu, C.C. Lin, X.K. Shen, Y. Ding, Y.L. Yu, C.Y. Mu, P. Liu, K.Y. Cai, Remote eradication of biofilm on titanium implant via near-infrared light triggered photothermal/photodynamic therapy strategy, Biomaterials 217 (2019) 119290.
[12] J. Tan, D.H. Wang, H.L. Cao, Y.Q. Qiao, H.Q. Zhu, X.Y. Liu, Effect of local alkaline microenvironment on the behaviors of bacteria and osteogenic cells, ACS Appl. Mater. Interfaces 10 (49) (2018) 42018–42029.
[13] Q.M. Luo, H.L. Cao, L.Y. Wang, X.H. Ma, X.Y. Liu, ZnO@ZnS nanorod-array coated titanium: good to fibroblasts but bad to bacteria, J. Colloid Interface Sci. 579 (2020) 50–60.
[14] X. Jin, Y.H. Xiong, X.Y. Zhang, R.X. Wang, Y.G. Xing, S. Duan, D.F. Chen, W. Tian, F.J. Xu, Self-adaptive antibacterial porous implants with sustainable responses for infected bone defect therapy, Adv. Funct. Mater. 29 (17) (2019) 1807915.
[15] L. Zhang, Y. Xue, S. Gopalakrishnan, K. Li, Y. Han, V.M. Rotello, Antimicrobial peptide-loaded pectolite nanorods for enhancing wound-healing and biocidal activity of titanium, ACS Appl. Mater. Interfaces 13 (24) (2021) 28764–28773.
[16] Z. Yuan, B.L. Tao, Y. He, J. Liu, C.C. Ling, X.K. Shen, Y. Ding, Y.L. Yu, C.Y. Mu, P. Liu, K.Y. Cai, Biocompatible MoS2/PDA-RGD coating on titanium implant with antibacterial property via intrinsic ROS-independent oxidative stress and NIR irradiation, Biomaterials 217 (2019) 119290.
[17] L. Tan, J. Li, X. Liu, Z. Cui, X. Yang, S. Zhu, Z. Li, X. Yuan, Y. Zheng, K.W.K. Yeung, Rapid biofilm eradication on bone implants using red phosphorus and nearinfrared light, Adv. Mater. 30 (31) (2018) 1801808.
[18] G.N. Zhang, Y.Q. Yang, J. Shi, X.H. Yao, W.Y. Chen, X.C. Wei, X.Y. Zhang, P.K. Chu, Near-infrared light II - assisted rapid biofilm elimination platform for bone implants at mild temperature, Biomaterials 269 (2021) 120634.
[19] J. Li, X.M. Liu, Z. Zhou, L. Tan, X.B. Wang, Y.F. Zheng, Y. Han, D.F. Chen, K.W. K. Yeung, Z.D. Cui, X.J. Yang, Y.Q. Liang, Z.Y. Li, S.L. Zhu, S.L. Wu, Lysozyme-assisted photothermal eradication of methicillin-resistant staphylococcus aureus infection and accelerated tissue repair with natural melanosome nanostructures, ACS Nano 13 (2019) 11153–11167.
[20] S. Yu, G. Li, P. Zhao, Q. Cheng, W. Xue, NIR-laser-controlled hydrogen-releasing PdH nanohydride for synergistic hydrogen- photothermal antibacterial and wound-healing therapies, Adv. Funct. Mater. 29 (50) (2019) 1905697.
[21] Y. Li, X.M. Liu, B. Li, Y.F. Zheng, Y. Han, D.F. Chen, K.W.K. Yeung, Z.D. Cui, Y. Q. Liang, Z.Y. Li, S.L. Zhu, X.B. Wang, S.L. Wu, Near-infrared light triggered phototherapy and immunotherapy for elimination of methicillin-resistant staphylococcus aureus biofilm infection on bone implant, ACS Nano 14 (2020) 8157–8170.

[22] K. Papenfort, B. Bassler, Quorum sensing signal-response systems in Gram-negative bacteria, Nat. Rev. Microbiol. 14 (2016) 576–588.

[23] J.E. Michaela, L.B. Bonnie, Snap Shot: bacterial quorum sensing, Cell 174 (2018) 1328, 1328.

[24] S.J. Cole, C.L. Hall, M. Schniederberend, J.M. Farrow, J.R. Goodson, E.C. Pesci, B. I. Kazmierczak, V.T. Lee, Host suppression of quorum sensing during catheter-associated urinary tract infections, Nat. Commun. 9 (2018) 4436.

[25] V.C. Kalia, S.K.S. Patel, Y. Kang, J. Lee, Quorum sensing inhibitors as antipathogens: biotechnological applications, Biotechnol. Adv. 37 (2019) 68–90.

[26] D.K. Ho, X. Murgia, C. De Rossi, R. Christmann, A.G. Hüfner de Mello Martins, M. Koch, A. Andreas, J. Herrmann, R. Müller, M. Empting, R.W. Hartmann, D. Desmaele, B. Loretz, P. Couvreur, C.M. Lehr, Squalenyl hydrogen sulfate nanoparticles for simultaneous delivery of tobramycin and an alkylquinolone quorum sensing inhibitor enable the eradication of P. aeruginosa biofilm infections, Angew. Chem. Int. Ed. 59 (2020) 10292–10296.

[27] D.L. Wang, J.Y. Shi, Y.N. Xiong, J.Y. Hu, Z.F. Lin, Y.L. Qiu, J.P. Cheng, A QSAR-based mechanistic study on the combined toxicity of antibiotics and quorum sensing inhibitors against Escherichia coli, J. Hazard Mater. 341 (2018) 438–447.

[28] Z. Yuan, C.C. Lin, L.L. Dai, Y. He, J.W. Hu, K. Xu, B.L. Tao, P. Liu, K.Y. Cai, Near-infrared light-activatable dual-action nanoparticle combats the established biofilms of methicillin-resistant Staphylococcus aureus and its accompanying inflammation, Small 17 (13) (2021) e2007522.

[29] Z. Yuan, C.C. Lin, Y. He, B.L. Tao, M.W. Chen, J.X. Zhang, P. Liu, K.Y. Cai, Near-infrared light-triggered nitric-oxide-enhanced photodynamic therapy and low-temperature photothermal therapy for biofilm elimination, ACS Nano 14 (3) (2020) 3546–3562.

[30] D.K. Joung, Y.S. Lee, S.H. Han, S.W. Lee, S.W. Cha, S.H. Mun, R. Kong, O.H. Kang, H.J. Song, D.W. Shin, D.Y. Kwon, Potentiating activity of luteolin on membrane permeabilizing agent and ATPase inhibitor against methicillin-resistant Staphylococcus aureus, Asian Pacific J. Tropical Med. 9 (2016) 19–22.

[31] Y.H. Sun, H.S. Qin, Z.Q. Yan, C.Z. Zhao, J.S. Ren, X.G. Qu, Combating biofilm associated infection in vivo: integration of quorum sensing inhibition and photodynamic treatment based on multidrug delivered hollow carbon nitride sphere, Adv. Funct. Mater. 29 (2019) 1808222.

[32] K.M.G. O'Connell, J.T. MHodgkinson, H.F. Sore, M. Welch, G.P.C. Salmond, D. R. Spring, Combating multidrug-resistant bacteria: current strategies for the discovery of novel antibacterials, Angew. Chem. Int. Ed. 52 (2013) 10706–10733.

[33] A. Hoppe, N.S. Guldal, A.R. Boccaccini, A review of the biological response to ionic dissolution products from bioactive glasses and glass-ceramics, Biomaterials 32 (2011) 2757–2774.

[34] K.F. Eichholz, S. Von Euw, R. Burdis, D.J. Kelly, D.A. Hoey, Development of a new bone-mimetic surface treatment platform: nanoneedle hydroxyapatite (nnHA) coating, Adv. Healthcare Mater. 9 (2020) 2001102.

[35] M. Mirkhalaf, J. Goldsmith, J.Y. Ren, A.K. Dao, P. Newman, A. Schindeler, M. A. Woodruff, C.R. Dunstan, Highly substituted calcium silicates 3D printed with complex architectures to produce stiff, strong and bioactive scaffolds for bone regeneration, Appl. Mater. Today 25 (2021) 101230.

[36] T. Nonoyama, L. Wang, M. Tsuda, Y. Suzuki, R. Kiyama, K. Yasuda, S. Tanaka, K. Nagata, R. Fujita, N. Sakamoto, N. Kawasaki, H. Yurimoto, J.P. Gong, Isotope Microscopic observation of osteogenesis process forming robust bonding of double network hydrogel to bone, Adv. Healthcare Mater. 10 (2021) 2001731.

[37] X.H. Huang, X. Guo, L.T. Qu, Z.W. Wu, T. Yu, Y.P. Jiao, C.R. Zhou, Gradient regulation of osteo-immune microenvironment by chitooligosaccharide-containing ion-doped mesoporous silica nanoparticles to accelerate osteogenesis, Appl. Mater. Today 23 (2021) 101067.

[38] Z.Q. Wang, L.C. Wang, N. Prabhakar, Y.X. Xing, J.X. Zhang, K.Y. Cai, CaP coated mesoporous polydopamine nanoparticles with responsive membrane permeation ability for combined photothermal and siRNA therapy, Acta Biomater 86 (2019) 416–428.

[39] Y. Leng, J. Chen, S. Qu, TEM study of calcium phosphate precipitation on HA/TCP ceramics, Biomaterials 24 (2003) 2125–2131.

[40] Z.C. Hu, Q. Tang, D.Y. Yan, G. Zheng, M.B. Gu, Z.C. Luo, C. Mao, Z.Y. Qian, W. F. Ni, L.Y. Shen, A multi-functionalized calcitriol sustainable delivery system for promoting osteoporotic bone regeneration both in vitro and in vivo, Appl. Mater. Today 22 (2021) 100906.

[41] K. Xie, Z. Zhou, Y. Guo, L. Wang, G.Y. Li, S. Zhao, X.M. Liu, J. Li, W.B. Jiang, S. L. Wu, Y.Q. Hao, Long-term prevention of bacterial infection and enhanced osteoinductivity of a hybrid coating with selective silver toxicity, Adv. Healthcare Mater. 8 (2019) 1801465.

[42] M. Zhang, J.T. Zhang, J.S. Chen, Y. Zeng, Z.H. Zhu, Y. Wan, Fabrication of curcumin-modified TiO₂ nanoarrays via cyclodextrin based polymer functional coatings for osteosarcoma therapy, Adv. Healthcare Mater. 8 (2019) 1901031.

[43] B. Ozcelik, K.K.K. Ho, V. Glattauer, M. Willcox, N. Kumar, H. Thissen, Poly (ethylene glycol)-based coatings combining low-biofouling and quorum-sensing inhibiting properties to reduce bacterial colonization, ACS Biomater. Sci. Eng. 3 (2017) 78–87.

[44] A. Taunk, R. Chen, G. Iskander, K.K.K. Ho, D.S. Black, M.D.P. Willcox, N. Kumar, Dual-action biomaterial surfaces with quorum sensing inhibitor and nitric oxide to reduce bacterial colonization, ACS Biomater. Sci. Eng. 4 (2018) 4174–4182.

[45] Y. Zou, K.Y. Lu, Y.C. Lin, Y. Wu, Y.R. Wang, L.H.Z. Li, C.B. Huang, Y.X. Zhang, J. L. Brash, H. Chen, Q. Yu, Dual-functional surfaces based on an antifouling polymer and a natural antibiofilm molecule: prevention of biofilm formation without using Biocides, ACS Appl. Mater. Interfaces 13 (2021) 45191–45200.

[46] X.H. Jia, I. Ahmad, R. Yang, C. Wang, Versatile graphene-based photothermal nanocomposites for effectively capturing and killing bacteria, and for destroying bacterial biofilms, J. Mater. Chem. B 5 (2017) 2459–2467.

[47] S.M. Yu, G.W. Li, R. Liu, D. Ma, W. Xue, Dendritic Fe₃O₄@Poly(dopamine) @PAMAM nanocomposite as controllable NO-releasing material: a synergistic photothermal and NO antibacterial study, Adv. Funct. Mater. 28 (2018) 1707440.

[48] J.Y. Wang, M.H. Sui, Z.F. Ma, H.W. Li, B.J. Yuan, Antibacterial performance of polymer quaternary ammonium salt–capped silver nanoparticles on Bacillus subtilis in water, RSC Adv. 9 (2019) 25667–25676.

[49] A. Szcześ, L. Hołysz, E. Chibowski, Synthesis of hydroxyapatite for biomedical applications, Adv. Colloid Interface Sci. 249 (2017) 321–330.

[50] J.E. Song, N. Tripathy, D.H. Lee, J.H. Park, G. Khang, Quercetin inlaid silk fibroin/hydroxyapatite scaffold promotes enhanced osteogenesis, ACS Appl. Mater. Interfaces 10 (2018) 32955–32964.

[51] Y. Ding, Z. Yuan, P. Liu, K.Y. Cai, R.R. Liu, Fabrication of strontium-incorporated protein supramolecular nanofilm on titanium substrates for promoting osteogenesis, Mater. Sci. Eng. C 111 (2020) 110851.

[52] Y. Ding, Y.S. Hao, Z. Yuan, B.L. Tao, M.Y. Chen, C.C. Lin, P. Liu, K.Y. Cai, A dual-functional implant with an enzyme-responsive effect for bacterial infection therapy and tissue regeneration, Biomater. Sci. 8 (2020) 1840–1854.

[53] D.J. Lee, H.C. Tseng, S.W. Wong, Z. Wang, M. Deng, C.C. Ko, Dopaminergic effects on in vitro osteogenesis, Bone Res. 3 (2015) 15020.